ICAS 2020 SHANGHAI
International Council of the Aeronautical Sciences
32nd Congress of the International Council of the Aeronautical Sciences
September 6-10, 2021
Pudong Shangri-La, Shanghai, China

ANALYSIS OF A WING-TIP-MOUNTED SMALL-SCALE PROPELLER CONFIGURATION UNDER NON-AXIAL INFLOW CONDITIONS

M. Cerny[1], N. Herzog[2] & C. Breitsamter[3]

[1,3]Technical University of Munich
[2]Rolls-Royce Deutschland Ltd & Co KG

Abstract

Regarding the design of the propeller propulsion system of small and medium-sized aircraft and UAVs there is still a need for an aerodynamic analysis of the specific flow characteristics of such vehicles, namely, the combination of small propeller dimensions and a wide range of inflow angles. In this work, a wing-tip-mounted propeller is analyzed both experimentally as well as by URANS calculations. Analyzed are the behavior of time-averaged aerodynamic reaction forces regarding thrust, lift, and pitching moment, the surface pressure along the wing contour, and the occurring flow field.

Keywords: Propeller, Drone, UAV, Wind Tunnel, URANS

1. Introduction

The number and importance of small and medium-sized propeller-driven aircraft for the aviation industry is increasing both in the frame of unmanned aerial vehicles (UAVs) as well as for applications for urban air mobility [4, 8]. While many works are published concerning the flight mechanics or system architectural aspects of such vehicles, there is still a demand concerning their aerodynamic characteristics. Generally speaking, in comparison to larger aircraft, they can be attributed with an outstanding capability of rapid and agile flight maneuvers, typically resulting in a wide range of inflow angles in relation to the propellers or even reversed inflow [1, 6].

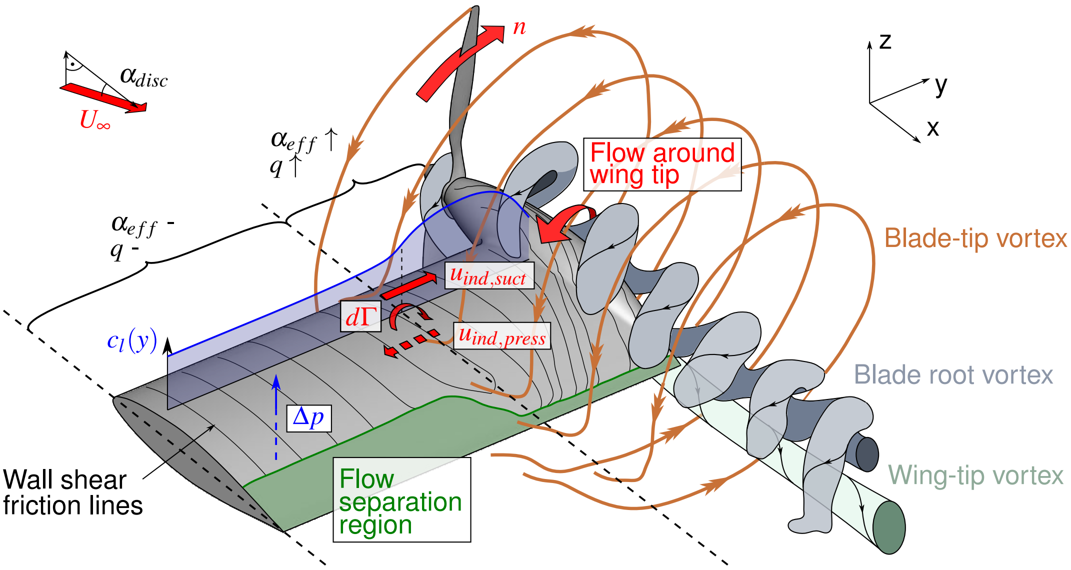

Figure 1 – Schematic illustration of the interference effects between the propeller and the wing element under a minor inflow angle, based on URANS results.

One feasible propulsion system for such vehicles is a puller propeller mounted at the tip of a short rotatable wing element. In this work, such a configuration is referred to as "WingProp" and will be analyzed with a special focus on high inflow angles. The occurring mutual interference effects of such a configuration are illustrated schematically in Figure 1 and described briefly in the following.

1.1 Upstream Effects

The wing's displacement causes both a blocking and an upwash effect, especially at the inboard portion of the propeller plane. Therefore, even under an inflow angle of $\alpha_{disc} = 0°$, the propeller faces non-uniform and non-axial local inflow conditions and produces cyclic load fluctuations. Additionally, Figure 1 shows the interruption of the blade tip and the blade root vortices. Under minor inflow angles, the root vortices are deflected towards the inflow direction. The resulting distance between them and the wing-tip vortex causes a complex wake structure with several vorticity cores of opposite sign.

1.2 Downstream Effects

The propeller influences the flow around the wing especially where the wing is covered by the propeller slipstream by increased dynamic pressure q and an increased effective angle of attack α_{eff}. Both result in a raised local lift production by the wing (see the trend of $c_l(y)$ in Figure 1). Additionally, the varied effective angle of attack may tilt the resultant force vector forward, decreasing the induced drag [7]. The lift gain in spanwise direction causes a local vortex shedding ($d\Gamma$) which in turn accelerates the flow towards the propeller on the wing's suction side ($u_{ind,suct}$) and away from the propeller on its pressure side ($u_{ind,press}$). Another effect is a delayed flow separation (illustrated by the green colored zone in Figure 1) and an increased viscous drag, caused by the additional dynamic pressure within the propeller slipstream [5].

2. Setup

To analyze the impact of higher inflow angles on these interference effects, the WingProp configuration is analyzed both experimentally in the wind tunnel and by unsteady Reynolds-averaged Navier-Stokes (URANS) simulations. The experimental and numerical simulation setups are described in the following.

2.1 Experimental Setup

The experiments are conducted in the wind tunnel A of the Chair of Aerodynamics and Fluid Mechanics of the Technical University of Munich. Its nozzle size reads 2.4 x 1.8 m, the length of the open test section 4.8 m. The maximum turbulence intensity is 0.4% with a maximum velocity of $U_\infty = 60$ m/s. The model features the two-bladed fixed-pitch propeller APC 18x8E. The symmetrical wing element shows the NACA 65A-019 profile, a fairing with the NACA 65A-020 profile surrounds the motor nacelle. At the trailing edge of the wing, a flap is implemented covering 25 % of the chord (see Figure 2). To separate the model from the floor boundary layer, a peniche of 125 mm height is used. At six spanwise locations, pressure taps are integrated along the chord to measure the static pressure, obtained by averaging over 30 seconds with a sampling rate of 200 Hz.

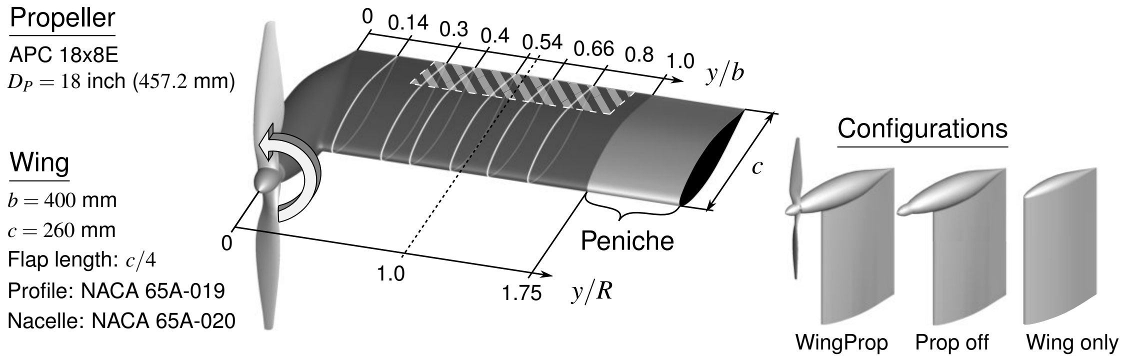

Figure 2 – Model geometry and locations of the pressure taps along six sections (white lines) relative to the span y/b and the propeller radius y/R. The hatched area represents the flap.

For all experiments, a transition strip of 0.145 mm height at around $x/c \approx 0.05$ on both the wing suction and the pressure side had been applied to enforce transition. Polar test measurements of different strip heights were performed. The current one was chosen since it showed the smoothest $c_L - \alpha$ trend before flow separation. In contrast, other strips showed secondary linear regimes.

For comparison, three model variants are analyzed: The WingProp model consists of the wing and the propeller, a propeller off configuration reveals the impact of its slipstream. In order to identify the influence of the engine nacelle, a configuration of a wing alone without the nacelle is tested as well (see Figure 2).

The propeller is driven by an electrical motor[1] which is mounted on an internal six-component balance[2] to measure solely the propeller loads. Its sampling rate is set to 3000 Hz. The whole assembly of wing and propeller is fixed on a wind tunnel underfloor balance[3], enabling the measurement of the wing loads by subtracting the propeller loads from the simultaneously measured total loads. All measurements are performed over thirty seconds to obtain the steady loads.

Referring to the chord length c and a kinematic viscosity of $\nu = 1.8 \cdot 10^{-5}$ Pa·s, the Reynolds number reads $Re_{Wing} = U_\infty c/\nu = 1.44 \cdot 10^5$ for an inflow velocity of $U_\infty = 10$ m/s. With a rotational velocity of $n = 4000$ rpm, the rotational blade tip Mach number reads about $Ma_{tip} \approx 0.28$.

2.2 Numerical Setup

The computational grid is created with the software ANSYS ICEM CFD and consists of two domains. An outer static domain contains the wing, the engine nacelle, and the wind tunnel floor and consists of 16.1 million cells. A cylindrical domain with the propeller blades is integrated in the outer one and consists of 4.2 million cells (see Figure 3). It rotates with the propeller at one degree per time step. Close to the wing and the blade surfaces, the grid is fine providing a dimensionless wall distance of $y+ < 0.9$ to resolve the turbulent boundary layer appropriately (see Figure 4).

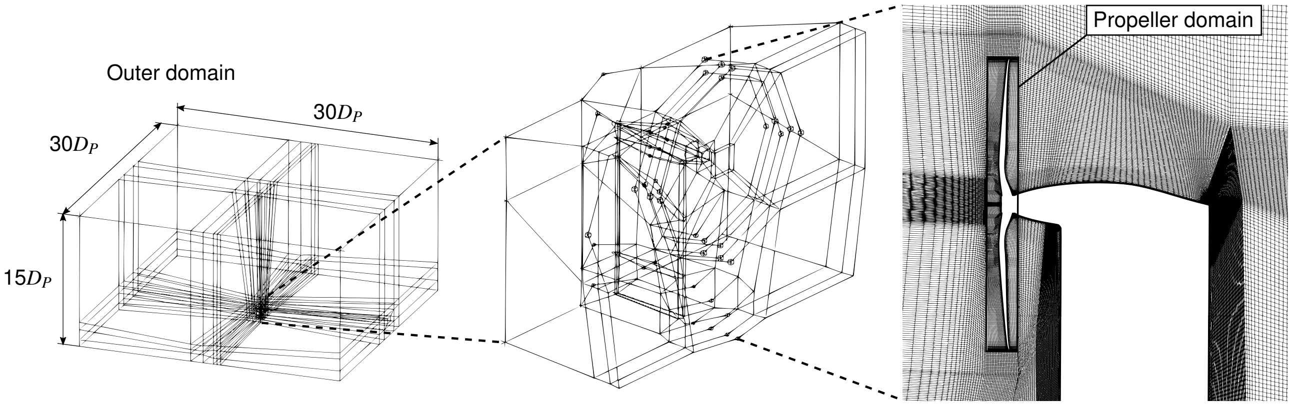

(a) (b) (d)

Figure 3 – Division of the domains and mesh at the symmetry plane.

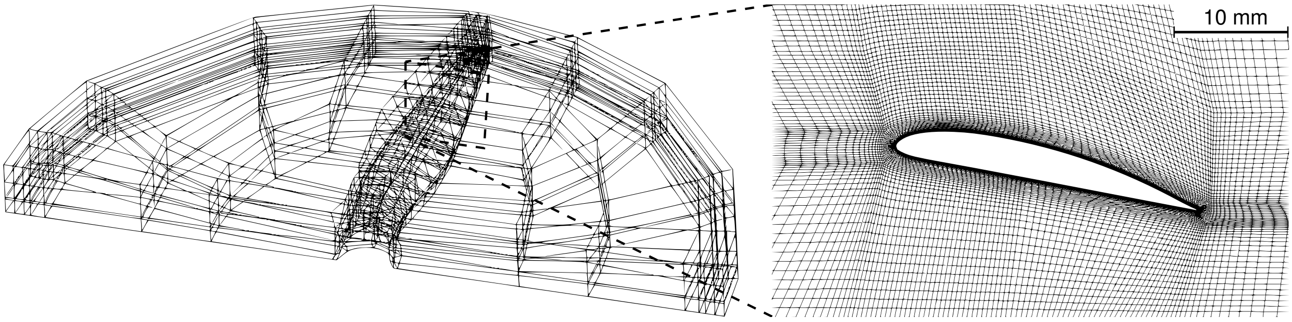

Figure 4 – Propeller domain and meshing at the blade section $r/R = 0.7$

---

[1] C54-1,5Y XL Acro 6,7:1 Competition Kv 1450, Hacker Motor GmbH.

[2] K6D-40, ME Messsysteme GmbH, resolution 0.5 N / 0.005 Nm.

[3] Resolution 0.375 N / 0.125 Nm

The incompressible URANS equations are solved with the software ANSYS Fluent applying the k-ω-SST turbulence model. The spatial and temporal gradients are discretized with the bounded second-order scheme. The simulation is performed over twenty propeller revolutions. To obtain the steady loads, the forces are averaged over the last revolution.

3. Results

In the following, the findings are presented, divided into the upstream and the downstream effects.

3.1 Upstream Effects on the Propeller

First, the upstream effects of the wing on the propeller under non-axial inflow are discussed, namely the impact on the steady (Sect. 3.1.1) and the transient thrust (Sect. 3.1.2). The characteristics of the pitching moment are discussed in Sect. 3.3.

3.1.1 Steady Propeller Thrust

In Figure 5, the static propeller thrust coefficient $c_{T,Prop} = T_{Prop}/(\rho n^2 D_P^4)$ is shown over the inflow angle α_{disc}, normalized with the propeller's rotational velocity n and its diameter D_P. The trend may be divided into five regions: Within the "linear regime" (L), a quasi-linear increase of the propeller thrust with α_{disc} can be observed mainly due to the decreased axial inflow component. The comparison with the thrust of an isolated propeller obtained from [3] reveals, that the upstream effect of the wing decreases $c_{T,Prop}$ slightly. Within the region between $\alpha_{disc} \approx 15°–30°$, flow separation and a delayed lift increase occurs at the wing surface which will be discussed later. Therefore, this region is referred to as "flow separation regime" (FS). The variations of the flow topology also affect the propeller thrust, resulting in fluctuations. Within the "post-stall regime" (PS, $\alpha_{disc} \approx 30°–110°$) a further quasi-linear increase of the propeller thrust can be observed. Nonetheless, increasing thrust fluctuations in this regime can be observed, for example by rising noise and vibrations during the wind tunnel experiments. Around $\alpha_{disc} \approx 120°$, a transition between the flow direction through the propeller disc occurs [3]. Within this "transition regime" (T), the thrust magnitude and the thrust fluctuations both reach their maxima. It is followed by the "reverse inflow regime" (R) where the thrust decreases again to a magnitude comparable to the conditions for $\alpha_{disc} \approx 70°$. Here, the propeller thrust suffers again from the presence of the wing. Additionally, the dependency of the propeller thrust on its rotational velocity is alternating. All trends become more constant with an increased n since the relative impact of the inflow U_∞ decreases with lower axial advance ratios. Considering the trend over the whole α_{disc} range, the results of the URANS calculations are in very good agreement with the experimental data. For a higher inflow velocity of $U_\infty = 25$ m/s (see Figure 5 right) and inflow angles of $\alpha_{disc} < 35°$, the propeller rotating with $n = 4000$ rpm operates in the "windmilling state" producing drag. In contrast, for a reversed inflow, the magnitudes of $c_{T,Prop}$ are increased in comparison to $U_\infty = 10$ m/s.

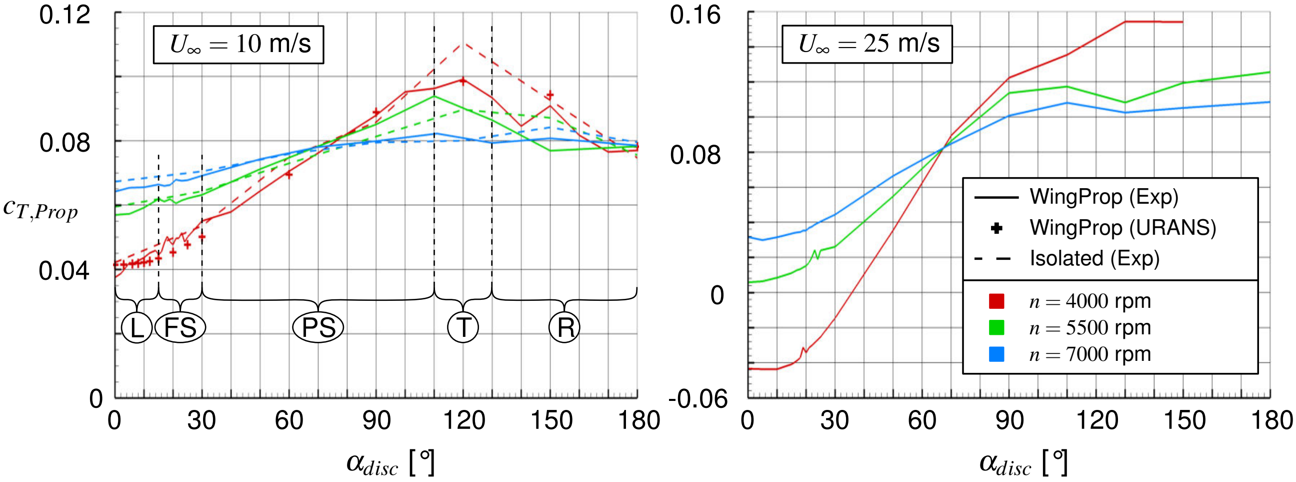

Figure 5 – Propeller thrust coefficient $c_{T,Prop}$ of the WingProp configuration and the isolated propeller over α_{disc}. Experiment and URANS data.

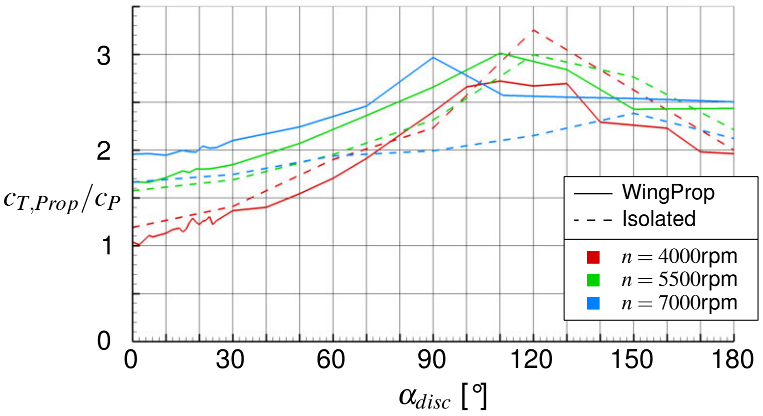

Figure 6 – Propeller thrust coefficient relative to power coefficient $c_{T,Prop}/c_P$ of the WingProp configuration and the isolated propeller over α_{disc}. $U_\infty = 10$ m/s. Experiment.

The ratio of the propeller's thrust coefficient to its power coefficient $c_P = P_{el}/(\rho n^3 D_P^5)$ can be used as an efficiency parameter and is obtained here by measuring the electrical input power of the motor controller P_{el}. Figure 6 shows, that for $n = 4000$ rpm the efficiency of the isolated propeller is higher than the one of the WingProp configuration for nearly all inflow angles. However, for $n = 5500$ rpm and $n = 7000$ rpm, the trend is the opposite and the WingProp configuration is more efficient. The higher the rotational velocity, the more the propeller benefits from the presence of the wing regarding its efficiency.

3.1.2 Transient Propeller Thrust

A major impact of the wing can be detected on the time-resolved propeller thrust. In Figure 7, the transient propeller thrust $c_T(\zeta)$ normalized with the respective steady propeller thrust is plotted over the propeller's azimuthal angle ζ as predicted by the URANS calculations. While for axial inflow ($\alpha_{disc} = 0°$), the isolated propeller barely shows any fluctuations, they reach up to two percent for the WingProp configuration.

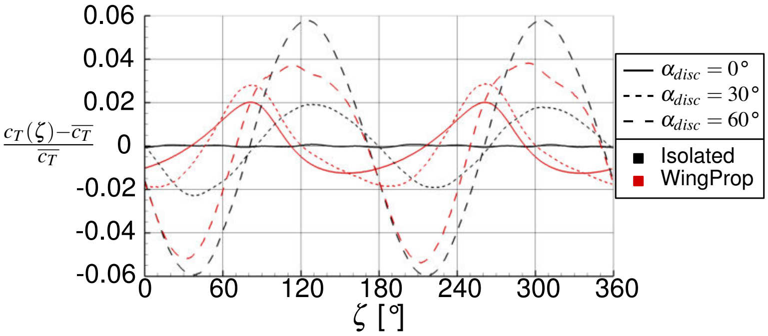

Figure 7 – Transient relative to mean propeller thrust $[c_T(\zeta) - \overline{c_T}]/\overline{c_T}$ over the propeller's azimuthal location ζ of the WingProp and the isolated propeller. $U_\infty = 10$ m/s, $n = 4000$ rpm, URANS.

On the other side, for a higher inflow angle of $\alpha_{disc} = 60°$, the relative magnitude of the propeller thrust fluctuation is significantly higher when the propeller is operated isolatedly. The reason for that is partly seen in the deflection of the flow by the wing. It increases the effective inflow angle and hence, reduces the axial inflow component at the propeller disc. The resulting increased steady propeller thrust lowers the relative magnitude of the fluctuations.

3.2 Downstream Effects on the Wing

In the following, the downstream effects of the propeller slipstream on the wing are discussed.

3.2.1 Static Pressure along the Chord

In Figure 8, the trend of the static pressure coefficient $c_P = (P - P_\infty)/(\rho/2\, U_\infty^2)$ along the normalized chord length x/c for $\alpha_{disc} = 15°$ is shown at six spanwise sections (see Figure 2). The numerical results are obtained from the last calculated time-step while the experimental ones show the time-averaged pressures.

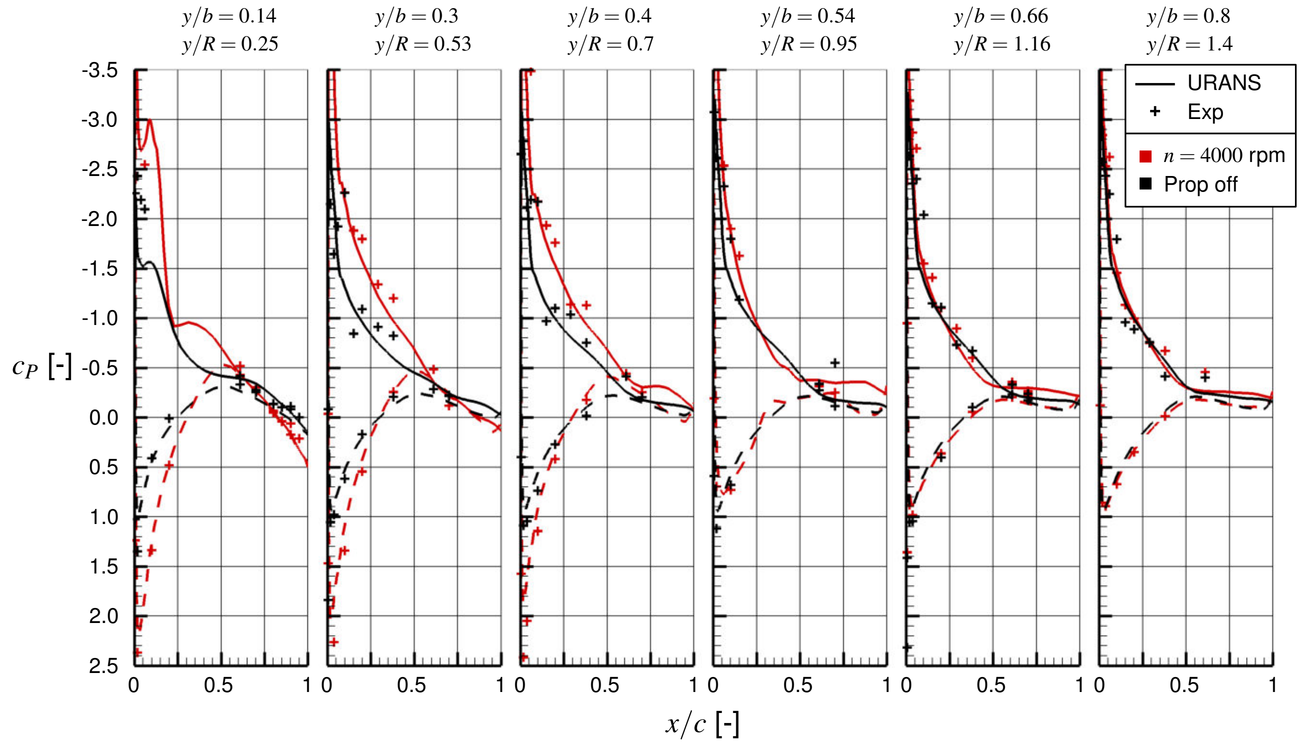

Figure 8 – Distribution of the static pressure coefficient c_P with and without propeller along the chord at six spanwise sections. $U_\infty = 10$ m/s, $\alpha_{disc} = 15°$. Experiment and URANS.

The comparison of the propeller off configuration and the conditions for $n = 4000$ rpm reveals a significant suction gain on the suction side of the wing downstream of the propeller disc ($y/b \leq 0.4$) both in numerical and experimental results. Additionally, one recognizes a delayed flow separation, while outside of the propeller swirl (at $y/R = 1.16$ and $y/R = 1.4$), a nearly constant suction level downstream of $x/c \approx 0.5$ indicates an earlier flow separation. On the pressure side of the wing, the pressure magnitudes of both high ($c_P > 0$) and low pressure regions ($c_P < 0$) are increased by the propeller swirl, but dominant is the increase of high pressure resulting in an increased lift production.

3.2.2 Sectional Lift Coefficient along the Span

The calculated static pressure distribution is integrated along the chord to obtain the trend of the sectional wing lift coefficient c_l along the span. Figure 9 shows the results for different inflow angles for the propeller off configuration and the conditions for $n = 4000$ rpm.

While the wing featuring a symmetrical airfoil alone produces no lift at no inclination, the increased dynamic pressure and the stagnation of the upwards-moving inboard propeller slipstream part on the wing's lower side forms a pressure difference Δc_P and hence, produces lift. This occurs especially downstream of the propeller disc, but outside of the slipstream, lift production can be detected as well.

For the inflow angles between $\alpha_{disc} = 10°–15°$, the discrepancy regarding the lift production of the propeller on and off conditions both inside but also outside the propeller slipstream reaches its maximum.

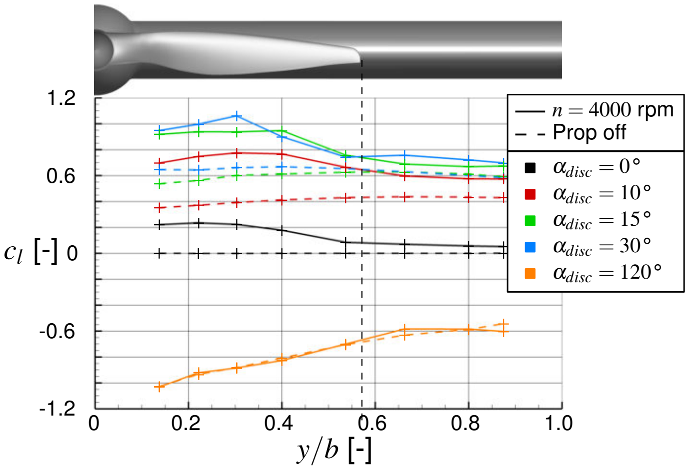

Figure 9 – Distribution of the sectional wing lift coefficient c_l along the span for $U_\infty = 10$ m/s and different inflow angles α_{disc}. URANS.

If the inflow angle is further increased to $\alpha_{disc} = 30°$, the downstream effect concerning lift production reduces again. And, for a very high inflow angle of $\alpha_{disc} = 120°$, no distinct influence of the propeller on the wing's lift production can be identified.

3.2.3 Integral Wing Lift

The integral lift of the wing is measured with the wind tunnel underfloor balance and normalized via two ways: $c_{L,Wing}$ is normalized according to the propeller operation similar to the steady propeller thrust. $\widetilde{c_{L,Wing}}$ is normalized with the inflow and wing span b and chord c:

$$c_{L,Wing} = L_{Wing}/(\rho n^2 D_P^4) \tag{1}$$

$$\widetilde{c_{L,Wing}} = L_{Wing}/(\rho/2\, U_\infty^2\, b\, c) \tag{2}$$

In Figure 10, $\widetilde{c_{L,Wing}}$ is plotted for an inflow velocity of $U_\infty = 10$ m/s over α_{disc} for all three model variants. The dashed line visualizes the trend of the wing only configuration and shows a quasi-linear increase within the "linear regime" (L). Then, flow separation occurs and the lift drops (FS). Within the "post-stall regime" (PS), $\widetilde{c_{L,Wing}}$ increases with the inflow angle and reaches its maximum at around $\alpha_{disc} \approx 45°$ before it decreases again, approaching the trend of a flat plate. Within the "transition" (T) and the "reverse inflow regime" (R) no strict correlation between wing lift and propeller rotational velocity can be observed, the trends are alternating. Additionally, especially within T, major discrepancies with the URANS results are apparent.

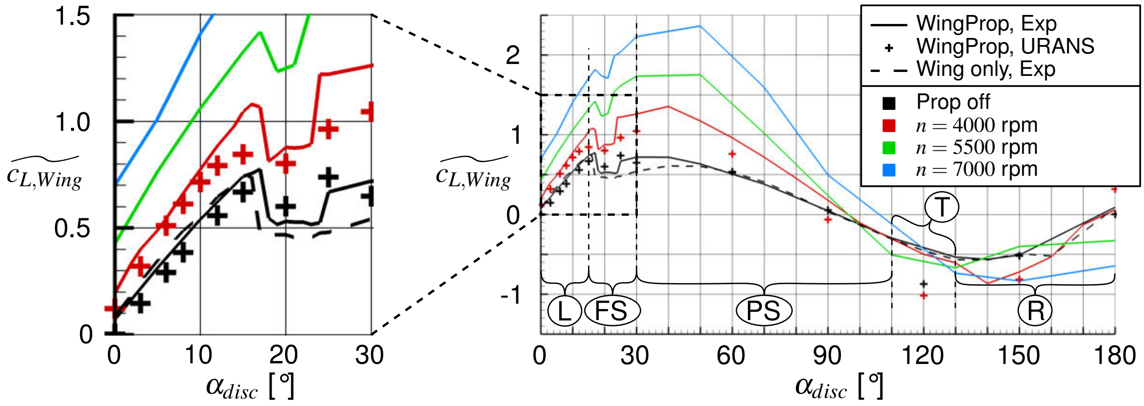

Figure 10 – Wing lift coefficient $\widetilde{c_{L,Wing}}$ of all three model variants over α_{disc}. $U_\infty = 10$ m/s, $Re_{Wing} = 1.44 \cdot 10^5$. Experiment and URANS.

The comparison with the propeller-off configuration shows the influence of the motor nacelle especially within FS and the beginning of the PS regime in the sense of a delayed flow separation at around $\alpha_{disc} \approx 17°$ and a sudden lift increase at around $\alpha_{disc} \approx 25°$.

While for the propeller-off configuration, both simulation methods agree in predicting these phenomena, for $n = 4000$ rpm, the URANS data does not show the lift increase in that extent. On the contrary, the experiments report an increased lift jump at $\alpha_{disc} = 25°$. Concerning that, Figure 11 shows the pressure coefficient discrepancy between the propeller-off conditions for $\alpha_{disc} = 20°$ and $25°$ over the wing contour as calculated by the URANS simulations. Besides a slight pressure increase on the wing's pressure side and a suction increase on its suction side, the highest discrepancy can be recognized around the motor nacelle. Therefore, the disagreement between the experimental and the numerical results is attributed to flow separation effects around the blunt nacelle body. There, small variations of the geometry during the manufacturing and the simplifications of the chosen turbulence model may have a significant impact on the results.

For the influence of an increasing rotational velocity of the propeller, the lift production of the wing significantly rises both for axial as well as non-axial inflow conditions (see Figure 10). However, the flow separation occurs at approximately $\alpha_{disc} \approx 17°$ for all rotational velocities as well as for the propeller-off condition. The Reynolds number increase by the propeller slipstream acceleration does not result in a detectable increased maximum of the linear angle of attack regime.

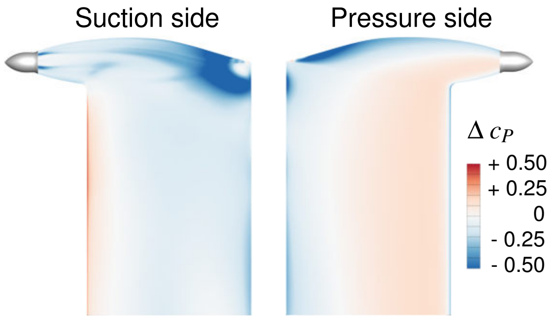

Figure 11 – Surface pressure variation correlated with the sudden lift increase $\Delta c_P = c_P(\alpha_{disc} = 25°) - c_P(\alpha_{disc} = 20°)$. Propeller-off conditions at one time-step. URANS.

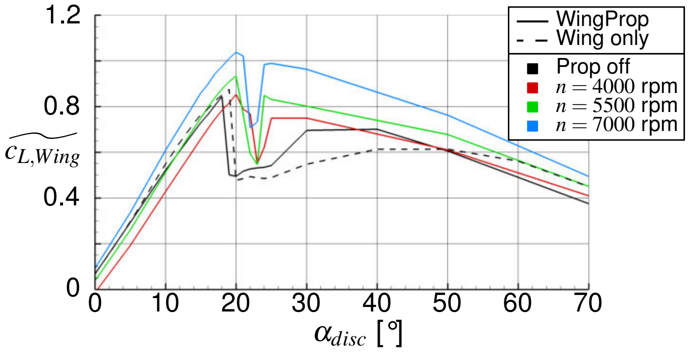

Figure 12 – Wing lift coefficient $\widetilde{c_{L,Wing}}$ of all three model variants over α_{disc}. $U_\infty = 25$ m/s, $Re_{Wing} = 3.6 \cdot 10^5$. Experiment.

The wing's lift behavior becomes different for an increased inflow velocity of $U_\infty = 25$ m/s resulting in a chord-based Reynolds number of $Re_{Wing} = 3.6 \cdot 10^5$ (see Figure 12). In general, flow separation occurs at higher inflow angles than for $U_\infty = 10$ m/s. However, in contrast to the lower inflow velocity, here, the propeller off configuration faces flow separation earlier than the wing only one. Again, all three analyzed rotational velocities result in flow separation at similar α_{disc}, but at higher incidence than for the wing only and the propeller-off configuration. Apparently, the propeller slipstream delays flow separation as an initial effect while the magnitude of the rotational velocity shows to have no significant influence. One also recognizes that the different rotational velocities affect the magnitude of $\widetilde{c_{L,Wing}}$ to a significantly lower extent than for $U_\infty = 10$ m/s due to the reduced relative flow acceleration by the propeller and the propeller thrust drop at higher U_∞. The latter phenomena explains why within the "linear regime" for $n = 4000$ rpm, the wing lift is even lower than without the propeller: The "windmilling state" occurs (see Figure 5).

3.2.4 The Effect of the Flap

The impact of the flap on the wing portion of the lift is illustrated in Figure 13 showing three different flap angles η. The wing only configuration shows the expected behavior of a nearly constant positive shift in lift within the linear lift regime followed by an earlier flow separation. For higher inflow angles, the effect of the flap decreases with rising α_{disc} and vanishes for $\alpha_{disc} \geq 60°$. For the propeller-off configuration, the lift gain by the flap shows to be less significant than for the wing only one.
For $n = 4000$ rpm, discontinuities can be observed when the flap is deployed prior to the occurrence of flow separation. Additionally, the flow separation is significantly delayed and flattened. Another phenomenon can be observed concerning the sudden lift increase at higher inflow angles. The more the flap is deployed, the earlier this lift gain occurs.

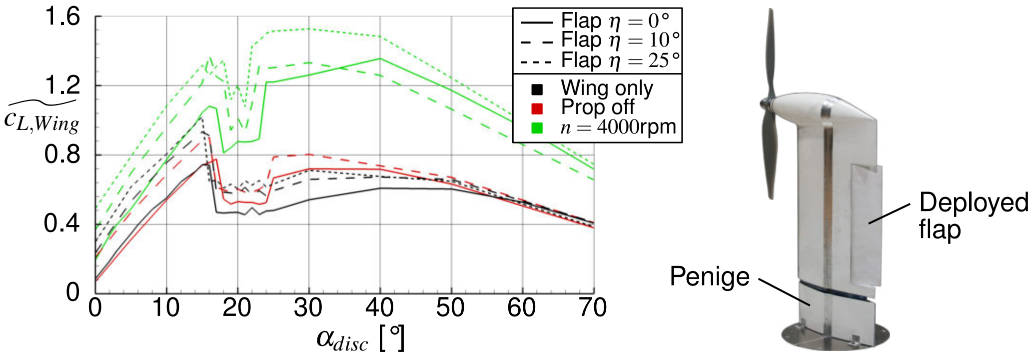

Figure 13 – Left: Wing lift coefficient $\widetilde{c_{L,Wing}}$ of all model variants and different flap angles over α_{disc}. $U_\infty = 10$ m/s. Experiment. Right: Photo of the WingProp configuration with extracted flap.

3.2.5 Lilienthal Polar

Figure 14 shows the Lilienthal polar featuring $\widetilde{c_{L,Wing}}$ over $\widetilde{c_{D,Wing}}$ for different model variants and flap angles. The mentioned flow separation delay effect of the propeller-off configuration in comparison to the wing only one can be seen. Furthermore, the propeller-off configuration produces more lift with the same drag between the inflow angle where flow separation occurs and medium high inflow angles ($\alpha_{disc} \approx 17°$–$50°$). For higher inflow angles, both configurations show similar characteristics.

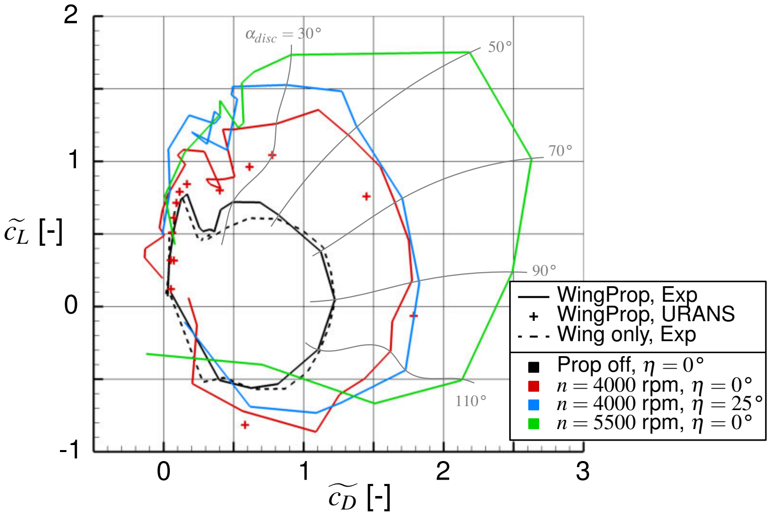

Figure 14 – Lilienthal polar showing the influence of the motor nacelle, the propeller's rotational velocity n, and the flap angle η. $U_\infty = 10$ m/s. Experiment.

A significantly high impact has the propeller slipstream. Note, that the trends in the plot showing propeller-rotating configurations are overlaid by noise since the low magnitude values of $\widetilde{c_{D,Wing}}$ are derived by subtracting the high magnitude propeller thrust from the measurements of the underfloor balance. Nonetheless, the trends can be investigated. Within the "linear regime", the accelerated flow of the slipstream increases particularly the lift of the wing. Here, the wing shows to have a negative drag (it effectively produces thrust) which may be attributed to the mentioned noise. Especially, the comparison of the URANS with the experimental data reveals significant deviations. The mentioned thrust production by the wing is not predicted by the numerical results.

Within the "flow separation regime", both the wing lift and drag are increased with a rising n. For $\alpha_{disc} \approx 50°–130°$, a faster propeller rotation gains primarily $\widetilde{c_{D,Wing}}$ while $\widetilde{c_{L,Wing}}$ is less affected.

The plot also contains the values of the configuration with a flap angle of $\eta = 25°$ for $n = 4000$ rpm. The data illustrate that the flap increases the lift especially within the "linear" and the "flow separation regime" without increasing the drag to a major extent.

3.3 Flight Mechanical Forces

For a flight mechanical description of a propulsion system, the forces in the aerodynamic coordinate system, namely the effective thrust in flight direction T_{eff}, the lift force L perpendicular to it, and the pitching moment m are of major importance (see Figure 15a). They are derived from the forces in the hub coordinate system by

$$\begin{pmatrix} -T_{eff} = D \\ L \end{pmatrix} = \begin{pmatrix} \cos\alpha_{disc} & \sin\alpha_{disc} \\ -\sin\alpha_{disc} & \cos\alpha_{disc} \end{pmatrix} \begin{pmatrix} -T \\ F_z \end{pmatrix} \tag{3}$$

To visualize the impact of a non-axial inflow on them and, in particular, to be able to distinguish the effect of an additional lateral inflow component (for example due to a gust) from the one of a rotation of the propulsion system, the loads are plotted over the here defined axial κ and lateral advance ratio μ (see Figure 15b) as a portion of the classical propeller advance ratio J by

$$\begin{pmatrix} \kappa \\ \mu \end{pmatrix} = J \begin{pmatrix} \cos\alpha_{disc} \\ \sin\alpha_{disc} \end{pmatrix} = \frac{1}{nD_P} \begin{pmatrix} U_x \\ U_z \end{pmatrix} \tag{4}$$

The contour plots contain all measured operating points, particularly the rotational velocities $n = \{4000, 5500, 7000\}$ rpm coupled with the inflow velocities $U_\infty = \{0, 10, 25\}$ m/s.

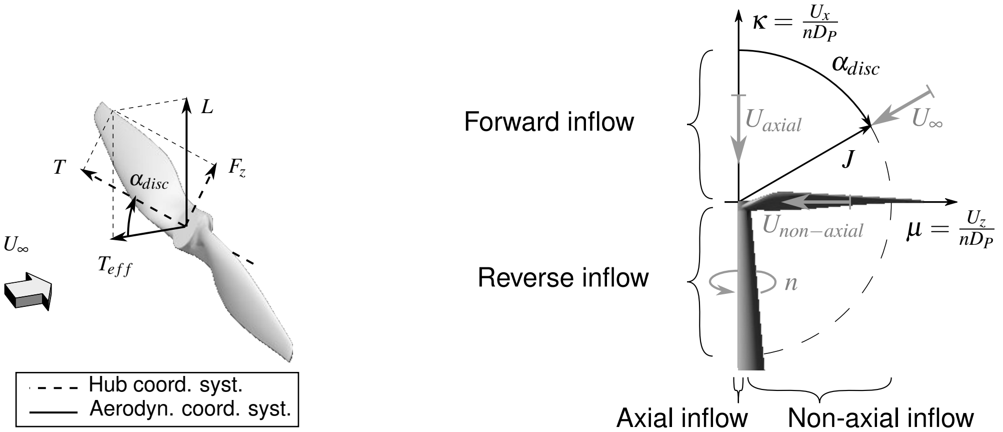

(a) (b)

Figure 15 – (a): Forces in the aerodynamic and the hub coordinate system. (b): Definition of the axial κ and lateral advance ratio μ [2].

In Figure 16, the effective thrust portion of the propeller, the wing (equaling its negative drag), and the whole WingProp configuration is plotted over κ and μ. Concerning the propeller portion (see Figure 16a), positive thrust shows to be limited by a maximum axial advance ratio of around $\kappa \approx 0.6$ representing the beginning of the "windmilling state" and a maximum angle of attack of around $\alpha_{disc} \approx 80°$ due to the rotation of the thrust vector away from the flight direction. Also, it is apparent that the effective thrust decreases with a rising lateral inflow, at least within the region of positive T_{eff}.

Regarding the wing portion, a significant dependency on κ cannot be found. Instead, $T_{eff,Wing}$ drops rapidly (or drag increases, respectively) with the non-axial inflow component.
The combination of both components (see Figure 16c) results in a narrowed region of positive effective thrust, namely the forward-oriented flight regime for low or medium-high inflow velocities.

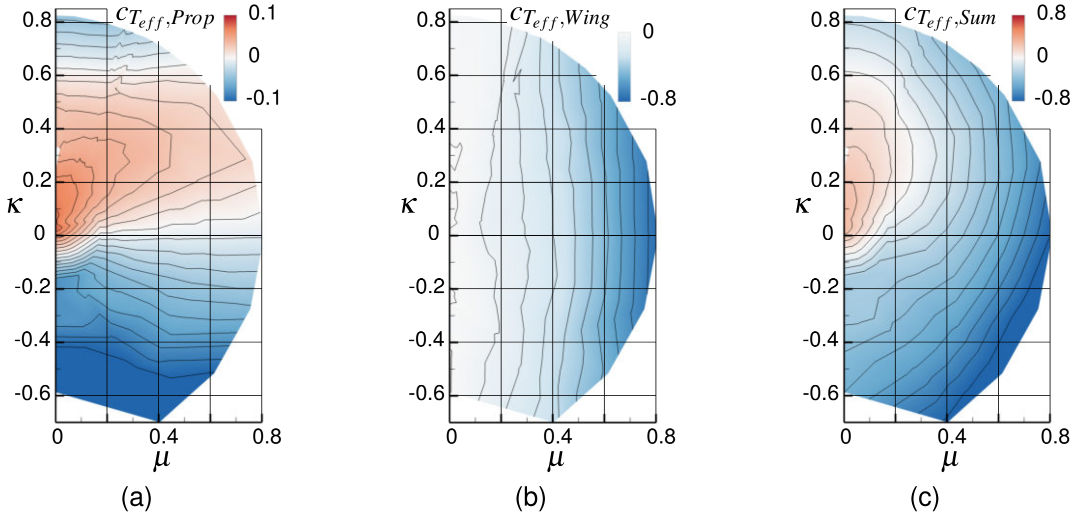

(a) (b) (c)

Figure 16 – Effective thrust coefficient $c_{T_{eff}}$ of (a) propeller, (b) wing, and (c) whole WingProp configuration over κ and μ. Experiment.

In Figure 17, the lift production of the WingProp configuration and its components is plotted over κ and μ. Regarding the propeller portion, a distinction has to be done between a forward- and a backward-oriented inflow. For the first, the propeller lift shows to be mainly dependent on the inflow angle whereas under the latter, it primarily depends on the lateral advance ratio. The maximum propeller lift occurs for $\alpha_{disc} \approx 110°$.
The plot of the wing portion of the lift (see Figure 17b) shows a complex behavior. For small inflow angles, it is dependent primarily on the lateral inflow. The discontinuity at around $\alpha_{disc} \approx 17°$ represents the flow separation impact. The more the inflow approaches a purely lateral inflow ($\alpha_{disc} \approx 90°$), the more the impact of the axial advance ratio increases significantly.
In combination with the propeller (see Figure 17c), the range of maximum lift is extended to higher inflow angles. Under smaller inflow angles, the wing produces the main portion of the lift, for higher inflow angles, the propeller becomes dominant.

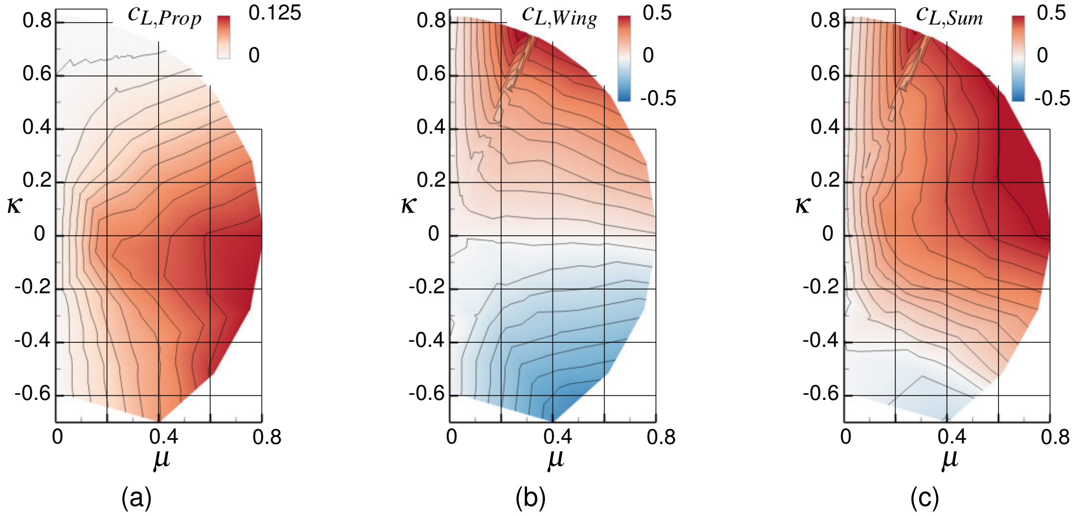

(a) (b) (c)

Figure 17 – Lift coefficient c_L of (a) propeller, (b) wing, and (c) whole WingProp configuration over κ and μ. Experiment.

One of the main consequences of non-axial inflow on propeller configurations is the production of a pitching moment m, caused mainly by the asymmetrical superposition of the non-axial inflow component $U_{\infty,z}$ with the circumferential velocity due to the propeller movement Ωr, causing an asymmetrical thrust production [3]. To quantify the relation between the propeller and the wing portion of the WingProp's pitching moment, Figure 18 shows them normalized by $c_m = m/(\rho n^2 D_P^5)$ over κ and μ. Due to the dependency on the asymmetrical influence of the non-axial inflow, the propeller portion shows a distinct dependency on the lateral advance ratio μ. The wing portion shows to be dependent on the advance ratio J and the inflow angle α_{disc}. The pitching moment increases drastically beyond the angle for which flow separation occurs and has its maximum at around $\alpha_{disc} \approx 50°$. Both components show comparable magnitudes. Therefore, the WingProp configuration produces in sum a pitching moment over a wide inflow angle regime.

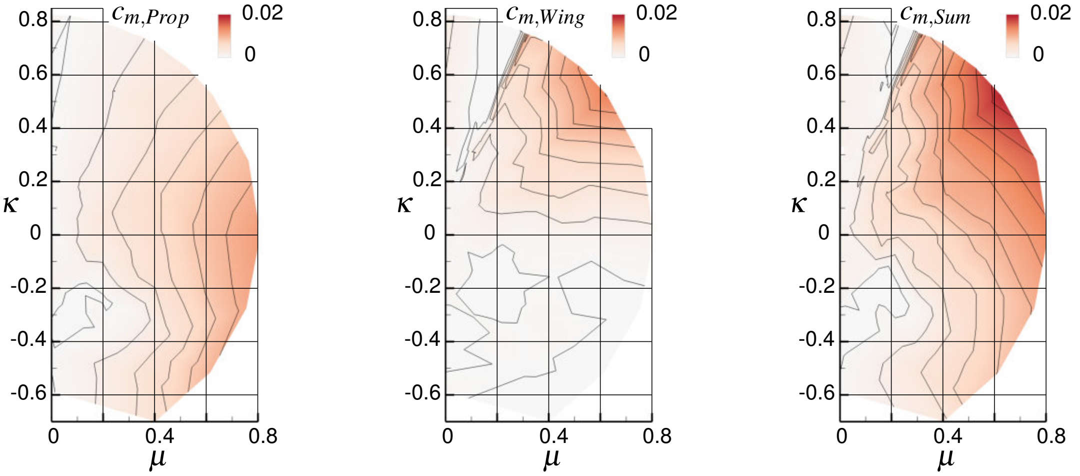

(a) (b) (c)

Figure 18 – Pitching moment coefficient c_m of (a) propeller, (b) wing, and (c) whole WingProp configuration over κ and μ. Experiment.

3.4 Flow Field Analysis

In Figure 19, flow field characteristics are shown for (a) an axial inflow for $U_\infty = 10$ m/s and (b) for a non-axial inflow of $\alpha_{disc} = 8°$. The conditions downstream of the motor nacelle are visualized by the vorticity component in x-direction $\omega_{x,norm} = \omega_x/\Omega$, normalized by the propeller's angular velocity Ω, and vectors following the in-plane flow directions in three sections. They show the behavior of the wing tip and the propeller blade root vortices as well as the swirl of the propeller slipstream. For an axial inflow, the wing tip vortex can be seen (in red) in the closest slice but already in the second one, a mutual reduction of the wing-tip and blade root vortices can be recognized which is beneficial for the induced drag. However, already for a minor inflow angle of $\alpha_{disc} = 8°$ (see Figure 19b), the discrepancy of both vortices in z-direction prevents a significant mutual reduction. Instead, the opposing rotational sense of both vortices results in an acceleration of the flow between them towards the inboard direction and a complex flow structure with secondary vortices is present. Due to the increased wing lift for $\alpha_{disc} = 8°$, the wing-tip vortex is increased significantly in strength.

The wing body surface flow highlights regions of negative wall shear stress in the x-direction indicating separated flow. Especially for $\alpha_{disc} = 8°$, one can recognize distinct regions of separated flow towards the trailing edge of the wing. However, the influence of the propeller slipstream in delaying flow separation is apparent. The wall streamlines illustrate the flow around the engine nacelle as well as the drift of the flow around the wing chord towards the center of the propeller slipstream due to the induction of the shed vorticity (see Figure 1).

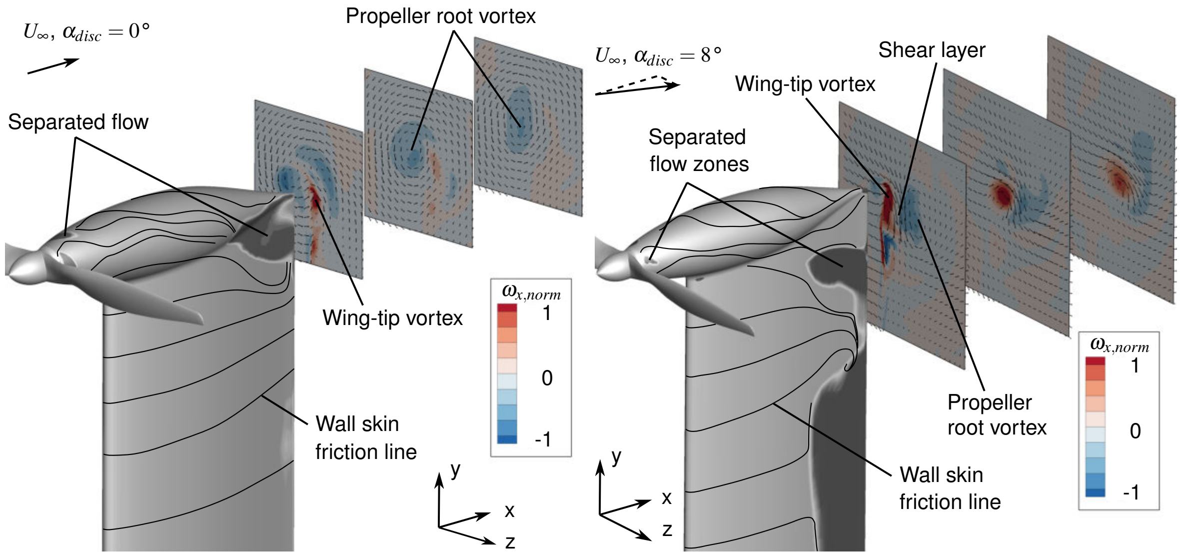

(a) (b)

Figure 19 – Normalized vorticity component in x-direction $\omega_{x,norm}$ at three sections and wall skin friction lines. URANS.

Figure 20 visualizes the flow field around the wing for $\alpha_{disc} = 15°$ at two sections by the normalized vorticity component in y-direction $\omega_{y,norm} = \omega_y/\Omega$ and the static pressure coefficient c_P.
The upper figures are attributed to $y/b = 0.4$ (or $y/R = 0.7$, respectively) placed through the propeller slipstream. One can identify an orientation of the flow along the propeller/chord-axis and flow separation occurring at the last 25 percent of the chord at this section location.

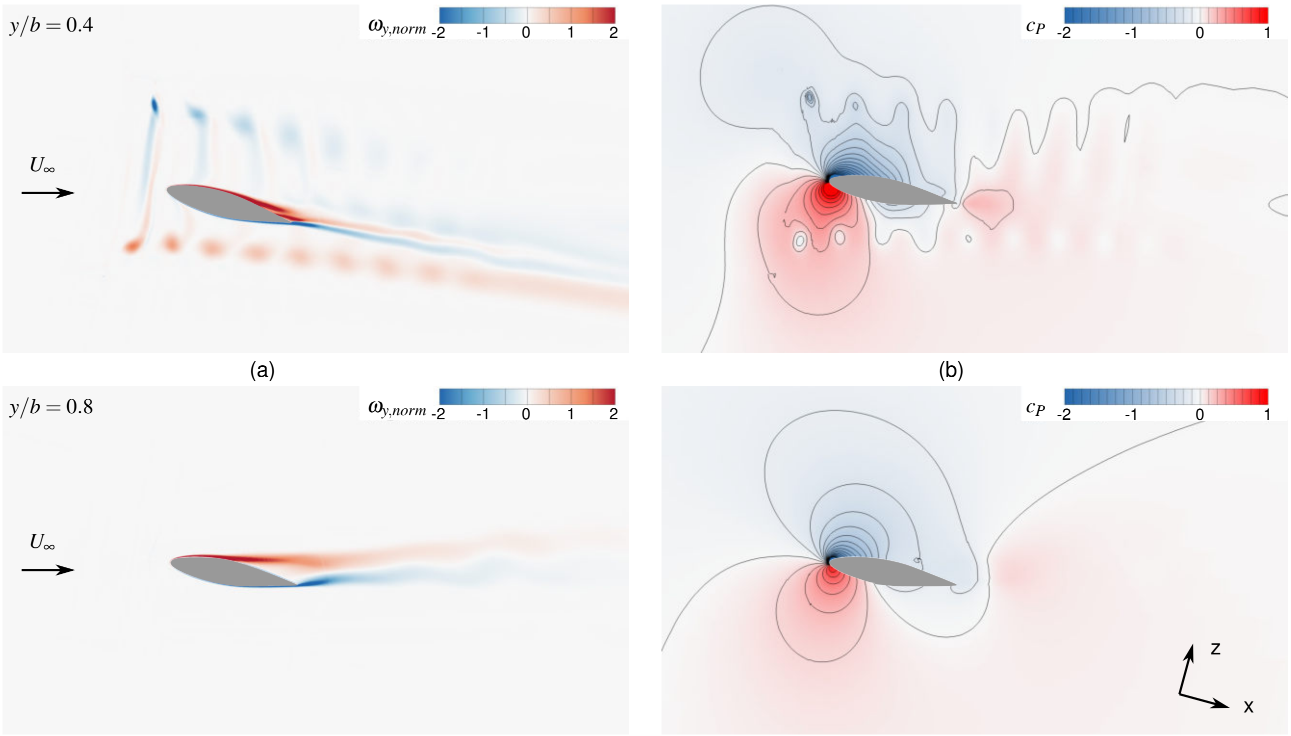

(a) (b)

(c) (d)

Figure 20 – (a,c): Normalized vorticity component in y-direction $\omega_{y,norm}$ and (b,d): static pressure coefficient c_P of the WingProp configuration at two sections. $U_\infty = 10$ m/s, $\alpha_{disc} = 15°$, $n = 4000$ rpm. URANS.

The lower figures are related to $y/b = 0.8$ (or $y/R = 1.4$, respectively) placed outside of the propeller slipstream. The comparison shows a much earlier flow separation and lower suction levels at the suction side of the wing while at its pressure side, the high pressure is decreased, responsible for the reduced sectional lift. These results agree with the experimental measurements of the surface pressure (compare Figure 8). They illustrate graphically the impact of the propeller slipstream in improving the aerodynamic characteristics of the wing performance.

4. Summary and Outlook

In this work, a wing-tip-mounted propeller configuration has been analyzed both experimentally and numerically via URANS simulations with a special focus on inflow conditions between $\alpha_{disc} = 0 - 180°$. It has been shown that the general effective thrust and lift characteristics of the wing-tip-mounted propeller configuration for the given propeller operating conditions are similar to an isolated propeller. Nonetheless, the wing decreases the magnitude of the thrust slightly. A distinct impact could be found concerning the transient propeller thrust. It becomes already periodically fluctuating at axial inflow in an extent that is comparable to the influence of non-axial inflow on an isolated propeller.

Further, it has been shown that the propeller slipstream delays flow separation and increases the sectional lift coefficient c_l even for medium-high inflow angles of $\alpha_{disc} = 30°$. For a reversed inflow of $\alpha_{disc} = 120°$, no significant influence on c_l could be found. Nonetheless, the mentioned flow separation delay does not significantly increase the maximum angle of attack of the linear regime of the integral wing lift production. In contrast to a wing only configuration, the behavior of all configurations with an engine nacelle showed a sudden lift increase at around $\alpha_{disc} \approx 25°$, even for the propeller off condition. The impact of a flap deflection has been studied and a significant lift increase with a higher propeller rotational velocity has been found while the drag increased only slightly. That appeared to be valid even for inflow angles up to $\alpha_{disc} = 40°$. For higher inflow angles ($\alpha_{disc} \geq 70°$) or reverse inflow, the effect of the flap vanished.

The contributions of the propeller and wing portions to the effective thrust in flight direction, the lift and the pitching moment production have been quantified for the whole inflow angle regime. It has been illustrated, which portion is responsible for the total flight mechanical loads.

Finally, the existence of a mutual reduction of the wing-tip and the propeller root vortices has been studied qualitatively for $\alpha_{disc} = 0°$ and $8°$. It showed, that under non-axial inflow conditions, the mutual interference of both results in complex flow field structures. Although the flow field with the wing-tip vortex might be affected in a beneficial way, secondary vortical structures might lead to higher power consumption by the propeller.

5. Acknowledgements

The authors would like to thank the Bavarian Research Foundation (Bayerische Forschungsstiftung) for funding the research project under the grant number AZ-1277-17. Further, we gratefully acknowledge the successful collaboration and support by the project partner Rolls-Royce Deutschland Ltd & Co KG. We give special thanks to ANSYS for providing the flow simulation software and the company APC Propellers for providing the geometrical data of the analyzed propeller.

6. Contact Author Email Address

For further information, please contact the authors under michael.cerny@tum.de.

7. Copyright Statement

References

[1] Bristeau, P-J, Martin P, Erwan S and Petit N. The Role of Propeller Aerodynamics in the Model of a Quadcopter UAV. *European Control Conference*, Budapest, Hungary, pp 683-688, 2009.

[2] Cerny M and Breitsamter C. Comparison of Isolated and Ducted Fixed-Pitch Propellers under Non-Axial Inflow Conditions. *Aerospace*, Vol. 7(8), No. 112, 2020.

[3] Cerny M and Breitsamter C. Investigation of Small-Scale Propellers under Non-Axial Inflow Conditions. *Aerospace Science and Technology*, Vol. 106, No. 106048, 2020.

[4] Leis, M (Fraunhofer Think Tank). Drones in Logistics. *Danish-German Drone R&D Workshop*, Munich, Germany, 2017.

[5] Sinnige T, van Arnhem N, Stokkermans T C A, Eitelberg G, Veldhuis L L M. Wingtip-Mounted Propellers: Aerodynamic Analysis of Interaction Effects and Comparison with Conventional Layout. *Journal of Aircraft*, Vol. 56, No. 1, pp 295-312, 2018.

[6] Theys B, Dimitriadis G, Andrianne T, Hendrick P and De Schutter J. Wind Tunnel Testing of a UAV MAV Propeller in Tilted Operating Mode. *International Conference on Unmanned Aircraft Systems (ICUAS)*, Orlando, FL, USA, pp 1064-1072, 2014.

[7] Veldhuis L L M. *Propeller Wing Aerodynamic Interference*. Diss., Delft University of Technology, 2005.

[8] Visiongain. Micro- Mini, Nano UAVs in Military, Homeland Security, Law Enforcement, Industrial, Media, Agriculture & Scientific Applications. *Small Unmanned Aerial Vehicles (UAV) Market Forecast 2015-2025*, 2015.